



## Article

# Study of Structural Transformation and Chemical Reactivity of Kaolinite-Based High Ash Slime during Calcination

Hongfei Xue , Xianshu Dong , Yuping Fan, Xiaomin Ma and Suling Yao

College of Mineral Processing Engineering, Taiyuan University of Technology, No. 79 Yingze West Street, Taiyuan 030024, China

\* Correspondence: dongxianshu@tyut.edu.cn

**Abstract:** The transformation of kaolinite into metakaolinite by thermal activation to obtain highly active aluminosilicate is commonly known. In addition to kaolin, the high content of kaolinite in coal mining waste is another potential source for obtaining an aluminosilicate precursor, thereby protecting the environment and adding value to industrial wastes. In this paper, the kaolinite-based high ash slime (KAS) was calcined at temperatures ranging from 400 °C to 1000 °C under air, N<sub>2</sub>, and CO<sub>2</sub> atmospheres, respectively. The thermal behaviors and structural evolution of each component in KAS were analyzed by thermal analysis (TG-DSC), X-ray diffraction (XRD), Fourier transform infrared spectroscopy (FTIR), and X-ray photoelectron spectroscopy (XPS). Moreover, the chemical reactivity of Al<sub>2</sub>O<sub>3</sub> and SiO<sub>2</sub> in calcined KAS was evaluated by HCl and NaOH leaching methods. The results show that the applied KAS in this study primarily consisted of kaolinite and carbon, while the minor mineral phases included quartz, calcite, and pyrite. Additionally, the structural transformation of kaolinite during calcination included dehydroxylation, sintering, and the formation of mullite. Crystalline kaolinite completely decomposed into semicrystalline metakaolinite at 600–800 °C, accounting for the increase in chemical reactivity. The interlayer sintering of metakaolinite and the recrystallization of amorphous components led to the decrease in chemical reactivity after 800 °C. Furthermore, the thermal behaviors of carbon in KAS are greatly affected by the calcination atmosphere. The presence of carbon reduced the chemical reactivity of calcined KAS.

**Keywords:** kaolinite-based high ash slime; thermal activation; calcination; structural transformation; chemical reactivity



**Citation:** Xue, H.; Dong, X.; Fan, Y.; Ma, X.; Yao, S. Study of Structural Transformation and Chemical Reactivity of Kaolinite-Based High Ash Slime during Calcination. *Minerals* **2023**, *13*, 466. <https://doi.org/10.3390/min13040466>

Academic Editor: Mercedes Suárez

Received: 17 February 2023

Revised: 22 March 2023

Accepted: 24 March 2023

Published: 26 March 2023



**Copyright:** © 2023 by the authors. Licensee MDPI, Basel, Switzerland. This article is an open access article distributed under the terms and conditions of the Creative Commons Attribution (CC BY) license (<https://creativecommons.org/licenses/by/4.0/>).

## 1. Introduction

Research studies based on clay minerals are currently receiving special attention from the scientific community. Clay minerals was widely used in the manufacture of construction materials such as cement, brick, concrete, and geopolymer [1–5], in the extraction of valuable elements and minerals [6–9], and in the preparation of engineered porous materials such as zeolites for separations and catalysis [10–13], etc. However, raw clay minerals with low chemical reactivity cannot be utilized directly in the aforementioned utilization. Thermal activation is an effective way to obtain high chemical reactivity precursors before further application [14–16].

The most common precursor source is kaolin. However, the shortage of high-quality kaolin has increased the necessity to seek new aluminosilicate materials as an alternative. Coal mining waste with a high clay minerals content is a potential source for obtaining an aluminosilicate precursor. Coal mining wastes are generated during coal washing and processing [17,18]. In 2020, the global coal production was 159.61 EJ [19]. The solid wastes generated during coal mining account for 10%–20% of coal production [16]. In China, the solid waste produced by the coal mining and washing industry were 468 million tons in 2020, accounting for 13.2% of the national general industrial solid waste production [20]. The coal-based solid wastes not only occupy land and pollute the environment, but also

cause serious economic losses to the coal industry [21,22]. Consequently, the developing trend of green mine construction in the coal industry and the concept of clean coal utilization require the comprehensive utilization of coal mining wastes [23,24].

Extensive studies have already demonstrated the effectiveness of calcined coal mining wastes. Zhang et al. [25] studied the thermal behavior of eight types of coal gangue mainly containing kaolinite, illite, and quartz. They found that the chemical reactivity mainly contributed to the transformation of kaolinite to metakaolinite, while illite plays a minor role and quartz is inert, suggesting that the optimal calcination temperature is 700 °C in the air atmosphere. Xu et al. [26] found that the mineral phase transformation from kaolinite to metakaolinite occurred at 500 °C. Likewise, Hollanders et al. [2] reported that all kaolinitic clays are highly reactive at a broad range of firing temperatures (500–900 °C). The reported optimal activation temperature of coal mining wastes varies in the literature. This determination appears complicated, which might be related to the differences in the type, content, and structure of clay minerals in the applied coal mining waste. It is known that kaolinite is highly reactive, and the optimal activation temperature of kaolinite is from 600–800 °C, while pure montmorillonite and illite possess optimal treatment temperature of 800 and 900 °C, respectively. Moreover, even at optimal firing temperatures, the reactivity of montmorillonite and illite are significantly smaller compared to that of kaolinite [2]. Therefore, it is necessary to thoroughly study the mineral composition of coal mining waste and its structural transformation in thermal activation.

Note that in addition to clay minerals, carbon is another important component that affects the chemical activity of coal mining waste during the calcination process. However, the understanding regarding the effects of carbon on the activation process was restricted to the fact that the extra heat provided by carbon for calcination promoted the decomposition of kaolinite [6,27]. Furthermore, the influence of the structural transformation of carbon under different calcination atmospheres and temperatures on the chemical reactivity of coal mining wastes has not been fully studied.

At present, the function of calcination not only involves the structural transformation of minerals but is also related to the combustion or carbonization of carbon in coal waste. The transformational features of each composition in coal mining waste affect the final chemical reactivity. Therefore, a kaolinite-based high ash slime (KAS) produced in the coal washing process was explored in this study.

This study mainly focuses on the influence of temperature and gas atmospheres on the structural transformation of carbon and minerals in KAS during calcination. Moreover, the leaching rate of  $\text{Al}_2\text{O}_3$  and  $\text{SiO}_2$  in KAS were determined by hydrochloric acid and sodium hydroxide leaching tests to evaluate the chemical reactivity of the calcined KAS. Finally, correlations between chemical reactivity and structural transformation were discussed to investigate the thermal activation mechanism. This research will provide significant theoretical guidance on the thermal activation of coal mining wastes.

## 2. Materials and Methods

### 2.1. Experimental Materials

The raw KAS used in this study was collected from the Xiegou coal preparation plant, located in Luliang City, Shanxi Province, China. The sample was ground and sieved to less than 0.125 mm, and then dried at 105 °C for 12 h. All chemicals used in this study were analytical pure and without any further purification.

### 2.2. Calcination Experiment

The optimal activation temperature of coal mining wastes reported in previous literature is between 500 and 900 °C [25,28]. Furthermore, a 2 h calcination time was sufficient to result in the structural changes, and a long calcination time decreased the reactivity of kaolinite [5,29]. In term of this knowledge, the KAS was heated up to the desired temperature (400, 500, 600, 700, 800, 900, or 1000 °C) at a heating rate of 10 °C·min<sup>−1</sup> in a tube furnace under a certain atmosphere (air, N<sub>2</sub>, or CO<sub>2</sub>) with a flow rate of 100 mL·min<sup>−1</sup>.

After being held for 2 h, the sample was cooled to room temperature with the tube furnace and finally placed in a desiccator for standby application. The calcined KASs are denoted as A-KAS-T, N-KAS-T, and C-KAS-T, where A, N, and C refer to air, N<sub>2</sub>, and CO<sub>2</sub> atmosphere, respectively, and T stand for the calcination temperature. For example, A-KAS-700 is the KAS calcined at 700 °C in air atmosphere for 2 h.

### 2.3. Determination of Active Al<sub>2</sub>O<sub>3</sub> and SiO<sub>2</sub> Contents

As reported in previous studies, the effectiveness of the thermal activation was determined by the calculated degree of amorphization indexes, which was calculated by characterizations, such as XRD [5], FTIR [28], and TGA [29]. These values proved to be useful indicators, but could not provide sufficient information [5]. In the present study, the effectiveness of thermal activation was determined by the measurement of active Al<sub>2</sub>O<sub>3</sub> and SiO<sub>2</sub> contents, which are those formed during the calcination, leachable by acid and alkali solutions, respectively [10,30,31].

The active Al<sub>2</sub>O<sub>3</sub> and SiO<sub>2</sub> contents of the different samples were obtained by first leaching 5 g of a calcined sample with 250 mL of a boiling 25 wt.% HCl solution, or with 250 mL of a boiling 25 wt.% NaOH solution, for 2 h, then filtering and washing the leached sample, and finally analyzing the filtrates by the ethylenediaminetetraacetic acid (EDTA) titration methods or the alkali-soluble carbon methods. The specific test methods are shown in the Supplementary Information (SI).

### 2.4. Characterizations

The moisture, ash, and volatile and fixed carbon contents were determined according to the National Standards of China GB/T 212-2008. The ultimate analysis of the KAS was conducted using a CHNS Elemental Analyzer (Vario EL, Elementar, Frankfurt, Germany). The chemical compositions of the residue ash, which is the KAS calcined at 900 °C for 3 h in a muffle furnace under the air atmosphere, were determined using an X-ray fluorescence spectrometer (XRF, 3600, Thermo Fisher, Waltham, MA, USA).

The mineral phases transformation of the KAS and calcined KAS was investigated by an X-ray powder diffractometer (XRD, miniflex600, Rigaku, Duzhaodao, Tokyo, Japan). The scanning range of 2θ was between 5° to 70°, with a step increment of 0.02° under the scan speed of 5°/min. The relative content of mineral compositions was determined by the semi-quantitative XRD analysis using the traditional reference intensity ratio (RIR) method.

Thermogravimetric analysis (TGA) and differential scanning calorimetry (DSC) were conducted using a simultaneous thermal analyzer (Model STA 449F3, NETZSCH, Selbu, Germany). The experimental condition was as follows: 10 mg KAS placed in the alumina crucible was heated from room temperature to 1000 °C at a heating rate of 10 °C/min. Another blank alumina crucible was simultaneously used as a reference. The measurements were performed in air, N<sub>2</sub>, and CO<sub>2</sub> atmospheres, respectively, at a flow rate of 60 mL·min<sup>−1</sup>.

To further investigate the structure transformation during thermal treatment, the infrared spectroscopic measurements were conducted on a Fourier transform infrared spectrometer (FTIR, VECTOR22, Bruker, Karlsruhe, Germany). Samples of 2 mg in size were mixed and ground with 200 mg KBr in an agate mortar, and then pressed into a 13.0 mm diameter pellet. The spectra were recorded in the range of 4000–500 cm<sup>−1</sup>, and the resolution was 4 cm<sup>−1</sup> with 32 scans.

The surface chemical states of silicon and aluminum in samples was elucidated by X-ray photoelectron spectroscopy (XPS, Axis Ultra<sup>DLD</sup>, KRATOS, Manchester, UK) with a monochromatic Al Kα source (1486.6 eV). The spectra were calibrated using the C1s spectrum at a peak of 284.8 eV.

### 3. Results and Discussion

#### 3.1. Essential Properties of KAS

The proximate and ultimate analyses of the KAS are shown in Table 1. The content of carbon in KAS was 26.16 wt.%, and the loss on ignition yields was 32.37 wt.%, which indicated that the organic carbon constituted KAS.

**Table 1.** Proximate and ultimate analyses of the kaolinite-based high ash slime (KAS).

Proximate Analysis, ad (wt.%)				Ultimate Analysis, ad (wt.%)			
M	A	VM	FC	C	H	N	S
0.60	67.63	17.36	14.41	26.16	2.95	0.42	1.40

Note: ad—air dry basis; M—moisture; A—ash yield; VM—volatile matter; FC—fixed carbon.

The main chemical composition of the KAS is listed in Table 2.  $\text{SiO}_2$  and  $\text{Al}_2\text{O}_3$  were the main constituents of the inorganic minerals in KAS, accounting for 32.17 wt.% and 27.75 wt.%, respectively. The ratio of  $\text{SiO}_2/\text{Al}_2\text{O}_3$  was 1.97, which was a little less than the theoretical value of kaolinite. Without special mention, the elemental content stated in this paper means the content in the KAS.

**Table 2.** Main chemical composition of the KAS.

$\text{SiO}_2$ (%)	$\text{Al}_2\text{O}_3$ (%)	CaO (%)	$\text{Fe}_2\text{O}_3$ (%)	$\text{SO}_3$ (%)	$\text{TiO}_2$ (%)	Others (%)	LOI (%)
32.17	27.75	2.70	2.19	1.00	0.89	0.93	32.37

The XRD pattern of the KAS is presented in Figure 1. The main minerals of the KAS were kaolinite, quartz, calcite, and pyrite. Two characteristic diffraction peaks appeared at  $2\theta = 12.3^\circ$  and  $2\theta = 24.8^\circ$ , which were attributed to the diffraction of (001) and (002) crystal planes of kaolinite ( $\text{Al}_2\text{O}_3 \cdot 2\text{SiO}_2 \cdot 2\text{H}_2\text{O}$ ), respectively. Meanwhile, the other characteristic peaks at  $2\theta = 19.8^\circ$ ,  $20.3^\circ$ , and  $23.0^\circ$  were due to the diffraction of (020), (110), and (111) crystal surface reflections of kaolinite, respectively. The characteristic diffraction peak for calcite was observed at  $2\theta = 29.4^\circ$ . In addition, the main peak of quartz at  $2\theta = 26.6^\circ$  and the peaks of pyrite at  $2\theta = 33.1^\circ$  and  $2\theta = 56.3^\circ$  were also detected.

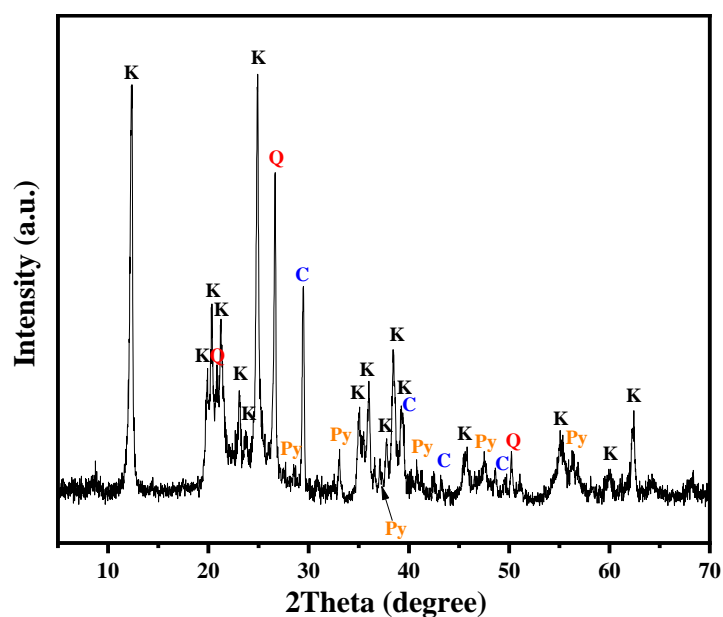


**Figure 1.** XRD pattern of the KAS (K—kaolinite, Q—quartz, C—calcite, Py—pyrite).

To accurately analyze the relative content of the minerals in KAS, the results of semi-quantitative XRD analysis are listed in Table 3. The results showed that kaolinite was the major mineral phase of the KAS, accounting for 77.5% of the several minerals, which was consistent with the high ratio of  $\text{Al}_2\text{O}_3/\text{SiO}_2$ .

**Table 3.** Mineral concentrations of the KAS.

Mineral	Kaolinite	Calcite	Quartz	Pyrite
Concentration (%)	77.5	7.2	10.0	5.7

The information on the molecular structure of KAS was revealed by FTIR spectra. From Figure 2, the characteristic peaks of kaolinite, quartz, calcite, and carbonaceous material can be observed. The assignments of characteristic absorption peaks of kaolinite are presented in Table 4. It can be seen that the absorption peaks at 3693, 3668, 3652, 3620, 938, 913, 797, 753, 694, 1621, 1033, 1009, 1114, 1097, and 538  $\text{cm}^{-1}$  were assigned to the OH, Si-O-Si, and Si-O-Al<sup>VI</sup> characteristic absorption vibrations of kaolinite.

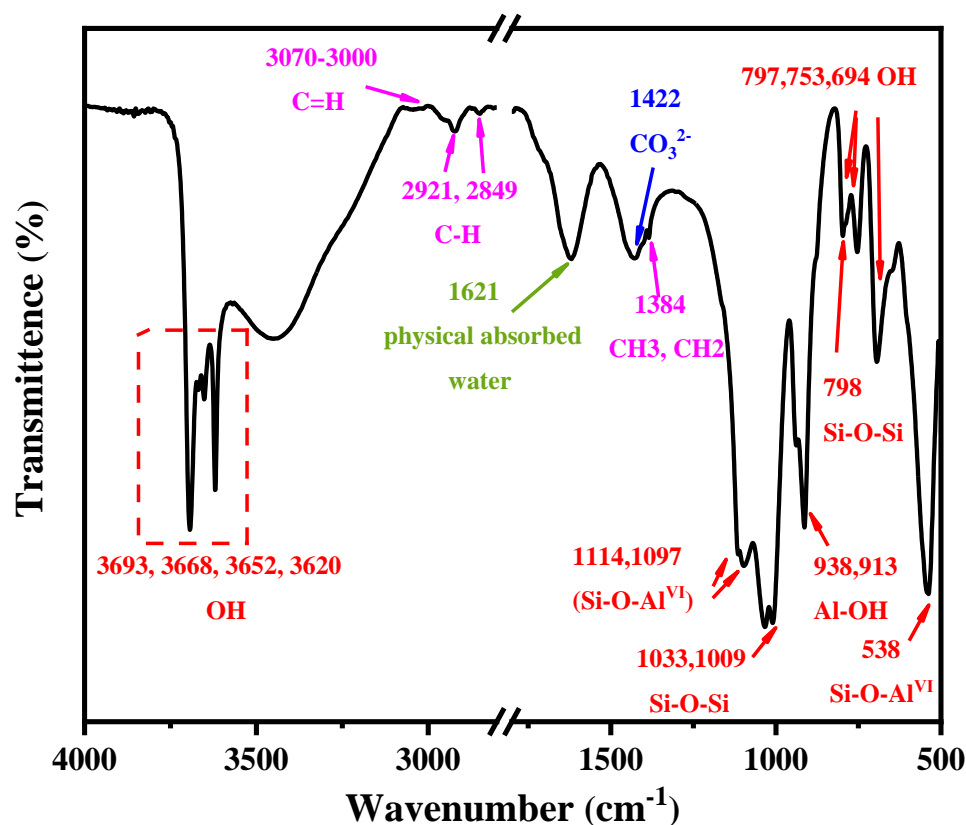


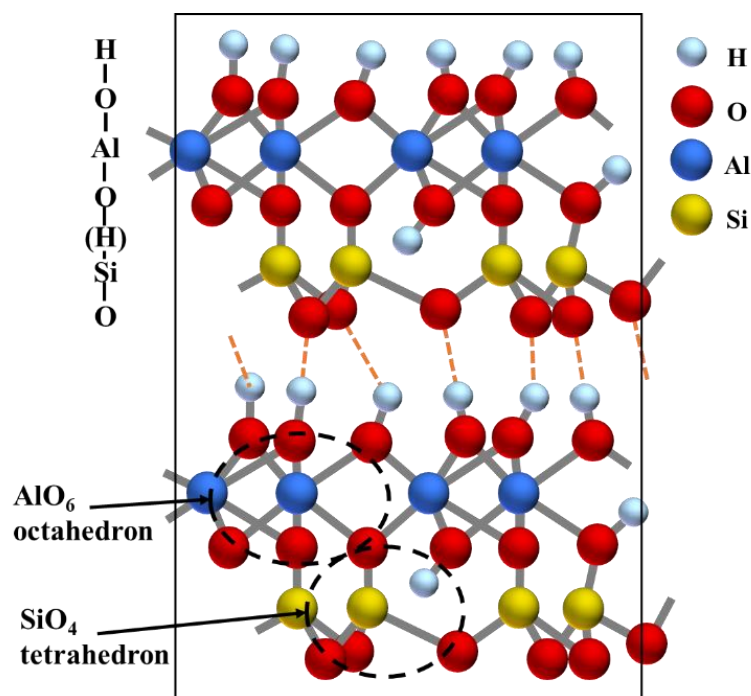
**Figure 2.** FTIR spectra of the KAS.

In addition to the characteristic peaks of kaolinite, the FTIR peak at 1422  $\text{cm}^{-1}$  corresponded to  $\text{CO}_3^{2-}$  asymmetric stretching vibration [32–34], which further proved the existence of calcite in the KAS. The feature bands of quartz at 1114, 1097, 797, 754, 695  $\text{cm}^{-1}$  were weak, which indicated that the content of quartz in KAS was much lower than that of kaolinite, corresponding to the results of XRD. Moreover, the bands at 3070–3000, 2921, 2849, and 1384  $\text{cm}^{-1}$  were assigned as carbonaceous matter vibration bands contained in the raw KAS.

**Table 4.** Characteristic absorption peaks of FTIR of kaolinite.

Assignment	Wavenumber (cm <sup>-1</sup> )	References
Outer OH stretching of Al <sup>VI</sup> -OH	3693, 3668, 3652	[2,25,26,35–37]
Inter OH stretching	3620	[2,25,26,36–38]
Outer OH bending of Al <sup>VI</sup> -OH	938	[7,25,26,35]
Inter OH bending	913	[7,25,26,34–36]
OH translation of Al <sup>VI</sup> -OH	797, 753, 694	[7]
Si-O-Si asymmetric stretching	1033, 1009	[34,39]
Si-O-Si symmetric stretching	798, 779	[25,26,34,35]
Si-O-Al <sup>VI</sup> stretching (apical Si)	1114, 1097	[25,26,35,38,40]
Si-O-Al <sup>VI</sup> deformation	538	[25,36,38,40]

Combined with the above analysis, it can be concluded that the studied KAS collected from the north of China is categorized in kaolinite-type clay coal waste. Figure 3 shows the layer structure of kaolinite. Kaolinite ( $\text{Al}_2\text{O}_3 \cdot 2\text{SiO}_2 \cdot 2\text{H}_2\text{O}$ ) is a 1:1 type layered aluminosilicate clay mineral. A layer of kaolinite is a structural unit consisting of a  $\text{SiO}_4$  tetrahedral sheet and an  $\text{AlO}_2(\text{OH})_4$  octahedral sheet. The two sheets are linked by Si-O-Al bonds and the inner hydroxyl groups. The inner hydroxyl groups share the plane with the apical oxygen atoms of the  $\text{SiO}_4$  tetrahedral structures. In addition, kaolinite contains another type of hydroxyl group, the outer hydroxyl group, which appeared in the outer surface of the  $\text{AlO}_2(\text{OH})_4$  octahedral sheet with the unshared plane. The unit layers are connected by outer hydroxyl groups and van der Waals forces.

**Figure 3.** Layer structure of kaolinite.

### 3.2. Thermal Analysis of KAS

Thermal analysis of the KAS is essential to understand the structural and chemical transformation of carbon and minerals during calcination [41]. The TG, DTG, and DSC curves of the KAS in different atmospheres are presented in Figure 4.

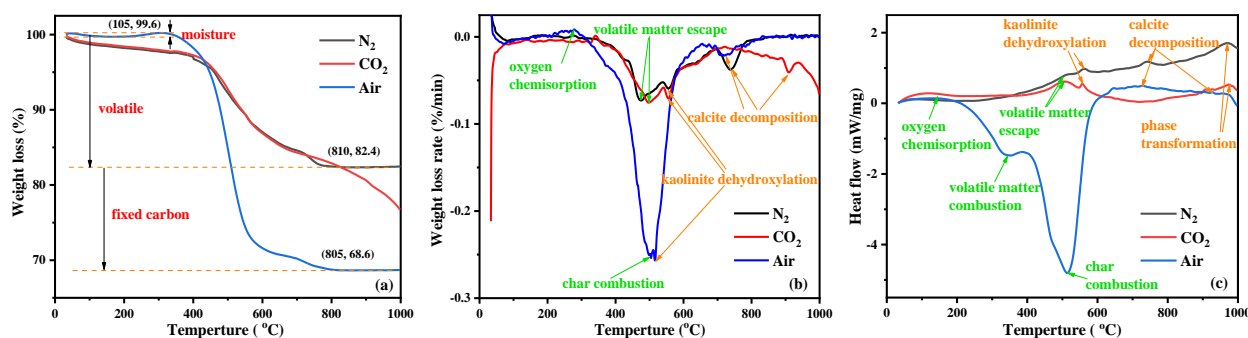


Figure 4. TGA (a), DTG (b), and DSC (c) curves of the KAS.

According to Figure 4a, the mass loss of the KAS was significantly different with temperatures under oxygen (air) and oxygen-free ( $N_2$  or  $CO_2$ ) atmospheres. Under  $N_2$  and  $CO_2$  atmospheres, the mass loss of the KAS calcined before  $800\text{ }^{\circ}\text{C}$  were about 17.4 wt.%, which was related to the moisture loss before  $105\text{ }^{\circ}\text{C}$  and the thermal decomposition of minerals and carbon. It was consistent with the content of moisture (0.67 wt.%) and volatile matter (17.36 wt.%) from a proximate analysis. Under air atmosphere, the mass loss increased by 13.8%, which was caused by the combustion of carbon, corresponding to the content of fixed carbon (14.41 wt.%) of the proximate analysis.

Under air atmosphere, the thermal behaviors of the KAS were mainly dominated by carbon combustion [42]. The features observed in the thermal curves of carbon in the KAS can be divided into three stages. The first stage is the oxygen physisorption and chemisorption between  $150\text{--}300\text{ }^{\circ}\text{C}$ , which resulted in a modest gain in mass and a slight exothermic peak. The second stage is the combustion of volatile matter in the range from  $200$  to  $400\text{ }^{\circ}\text{C}$ . The third stage is the combustion of fixed carbon between  $400$  and  $650\text{ }^{\circ}\text{C}$ . The combustion of volatile matter and fixed carbon caused a large weight loss of up to 29.5% on the TG curve and two exothermic peaks on the DSC curve. The processes of the carbon reacting with  $O_2$  can possibly be described in reactions (SI 10–14).

Compared to combustion, the thermal behaviors of the carbon, under both  $N_2$  and  $CO_2$  atmospheres, had only one stage of devolatilization ( $200\text{--}550\text{ }^{\circ}\text{C}$ ) before  $800\text{ }^{\circ}\text{C}$ . In this stage, there was a relatively lower weight loss and exothermic peak, indicating that carbon remained during the heating of the KAS under oxygen-free atmospheres [24]. After  $800\text{ }^{\circ}\text{C}$ , the thermal behaviors of the carbon under the  $CO_2$  atmosphere showed the second stage of char gasification leading to further weight loss [43], represented by the reaction (SI 15).

Moreover, the thermal decomposition processes were slightly different before  $800\text{ }^{\circ}\text{C}$  under the two oxygen-free atmospheres. From Figure 4a,b, the weight loss of the KAS under the  $N_2$  atmosphere was higher than that under the  $CO_2$  atmosphere, and the devolatilization peak temperature in the  $N_2$  atmosphere ( $472\text{ }^{\circ}\text{C}$ ) was lower than that in the  $CO_2$  atmosphere ( $498\text{ }^{\circ}\text{C}$ ). This was because the specific heat capacity of  $CO_2$  is higher than that of  $N_2$ , which resulted in a lower surface temperature of the KAS under the  $CO_2$  atmosphere than that under the  $N_2$  atmosphere. Thus, the escape of volatile matter required a higher temperature in the  $CO_2$  atmosphere [24,43].

In addition to carbon, the thermal behaviors of kaolinite and calcite in the KAS were also observed from Figure 4. Under  $N_2$  and  $CO_2$  atmospheres, a certain weight loss peak and a significant endothermic peak were observed around  $550\text{ }^{\circ}\text{C}$ , which were primarily attributed to the thermal decomposition of kaolinite [26,44]. However, under air atmosphere, the slight weight loss peak of the thermal decomposition of kaolinite shifted to a low temperature ( $510\text{ }^{\circ}\text{C}$ ), and the endothermic peak of kaolinite decomposition was not observed. This was because the decomposition of kaolinite occurred at the same stage as the combustion of carbon, and the heat generated by the combustion of carbon accelerated the decomposition of kaolinite [25,27]. As the temperature increased, a mild exothermal peak was observed at  $950\text{ }^{\circ}\text{C}$  on the DSC curve of each atmosphere, and there was no mass

loss on the TG curve under the same temperature range, which was a sign of the new aluminosilicate crystalline phase formation [25].

Under air, N<sub>2</sub>, and CO<sub>2</sub> atmospheres, the decomposition temperatures of calcite were 717, 740, and 910 °C, respectively. The decomposition resulted in a small weight loss and a tiny exotherm. It can be seen that the thermal decomposition of calcite was greatly influenced by the atmosphere. Particularly under the CO<sub>2</sub> atmosphere, the decomposition temperature of calcite was 170 °C higher than that under the N<sub>2</sub> atmosphere (Figure 4b) [24].

### 3.3. Mineral Transformation of KAS during Calcination

To investigate the possible mineral transformation and structural evolution during calcination, the XRD patterns and FTIR spectra of calcined KAS at 400 °C to 1000 °C under different atmospheres are presented in Figures 5 and 6, respectively.

From Figure 5, it can be seen that the calcination temperature and atmosphere had a great influence on the decomposition of minerals in the KAS. Quartz was stable during calcination; however, kaolinite, pyrite, and calcite showed different residual structures as a function of temperature under the three calcination atmospheres. To quantify, the relative decomposition rate of the three minerals was calculated using the change in the intensity of the diffraction peak of kaolinite, pyrite, and calcite relative to the intensity of the peak of quartz, respectively [6]. The formula is listed as follow:

$$\alpha = [1 - (I_x/I_Q)_{\text{calcined}} / (I_x/I_Q)_{\text{raw}}] \times 100\% \quad (1)$$

where  $\alpha$  is the relative decomposition rate,  $I_x$  can be  $I_K$ ,  $I_P$ , and  $I_C$ , representing the intensity of the diffraction peaks of kaolinite, pyrite, and calcite, respectively. In addition,  $I_Q$  is the peak intensity of quartz.

The calculation result is shown in Figure 7. From Figures 5 and 7, the characteristic peaks of kaolinite in the KAS calcined at 400 °C were still quite clear under N<sub>2</sub> and CO<sub>2</sub> atmospheres, while under air atmosphere, it dropped by 64.1%. Besides, the peaks of kaolinite in the KAS calcined at 500 °C almost vanished under air atmosphere, and the decomposition rate was 91.5%, but under N<sub>2</sub> and CO<sub>2</sub> atmospheres, the decomposition rates were only 66.7% and 38.1%, respectively. Moreover, the complete decomposition of kaolinite was achieved at 600 °C under each atmosphere. The results were consistent with the TGA-DTG-DSC analysis, indicating that compared with N<sub>2</sub> and CO<sub>2</sub> atmospheres, air atmosphere was more conducive to the low-temperature decomposition of kaolinite.

As for kaolinite, the combustion of carbon also contributed to the decomposition of pyrite and calcite, so at the same calcination temperature, the decomposition rate of pyrite and calcite under air atmosphere was highest than that under N<sub>2</sub> and CO<sub>2</sub> (Figure 7b,c). Moreover, the decomposition of calcite was also restrained by the CO<sub>2</sub> atmosphere, which was because the decomposition of calcite is very sensitive to the partial pressure of CO<sub>2</sub>, and the higher partial pressure of CO<sub>2</sub> in the system pushed the decomposition of calcite towards a higher temperature. The decomposition reactions of pyrite and calcite are show in (SI 16–17).

In addition, the FTIR analysis further proved the structural transformation from kaolinite to metakaolinite (Figure 6). From 400 °C to 600 °C, the gradual disappearance of the OH stretching vibrations at 3600–3700 cm<sup>−1</sup>, the OH bending vibrations at 900–950 cm<sup>−1</sup>, and OH translation vibrations at 650–800 cm<sup>−1</sup> indicated that OH was completely removed by calcination. Moreover, the peak disappearance rate of 3620 cm<sup>−1</sup> was faster than the peaks at 3693, 3668, and 3652 cm<sup>−1</sup>, which showed that the external hydroxyl group was easier to escape than the internal hydroxyl group. Meanwhile, the sharp Si-O and Al-O stretching bands at 1150–1000 cm<sup>−1</sup> became weaker and combined into a broad peak, and the position of the broad peak redshifted to 1520–1000 cm<sup>−1</sup>, indicating that the degree of crystallinity of kaolinite decreased. It was also observed that while the Si-O-Al<sup>VI</sup> stretching vibration peak at 538 cm<sup>−1</sup> disappeared, a new Si-O-Al<sup>IV</sup> peak appeared at 876 cm<sup>−1</sup>, which showed that the VI-coordinated aluminum in kaolinite was transformed to IV-coordinated aluminum in metakaolinite. The above all confirmed the transformation from crystalline

kaolinite to semicrystalline metakaolinite by dehydroxylation. The reaction and mechanism schematic diagram of this transformation are shown in SI 18 and Figure 8, respectively.

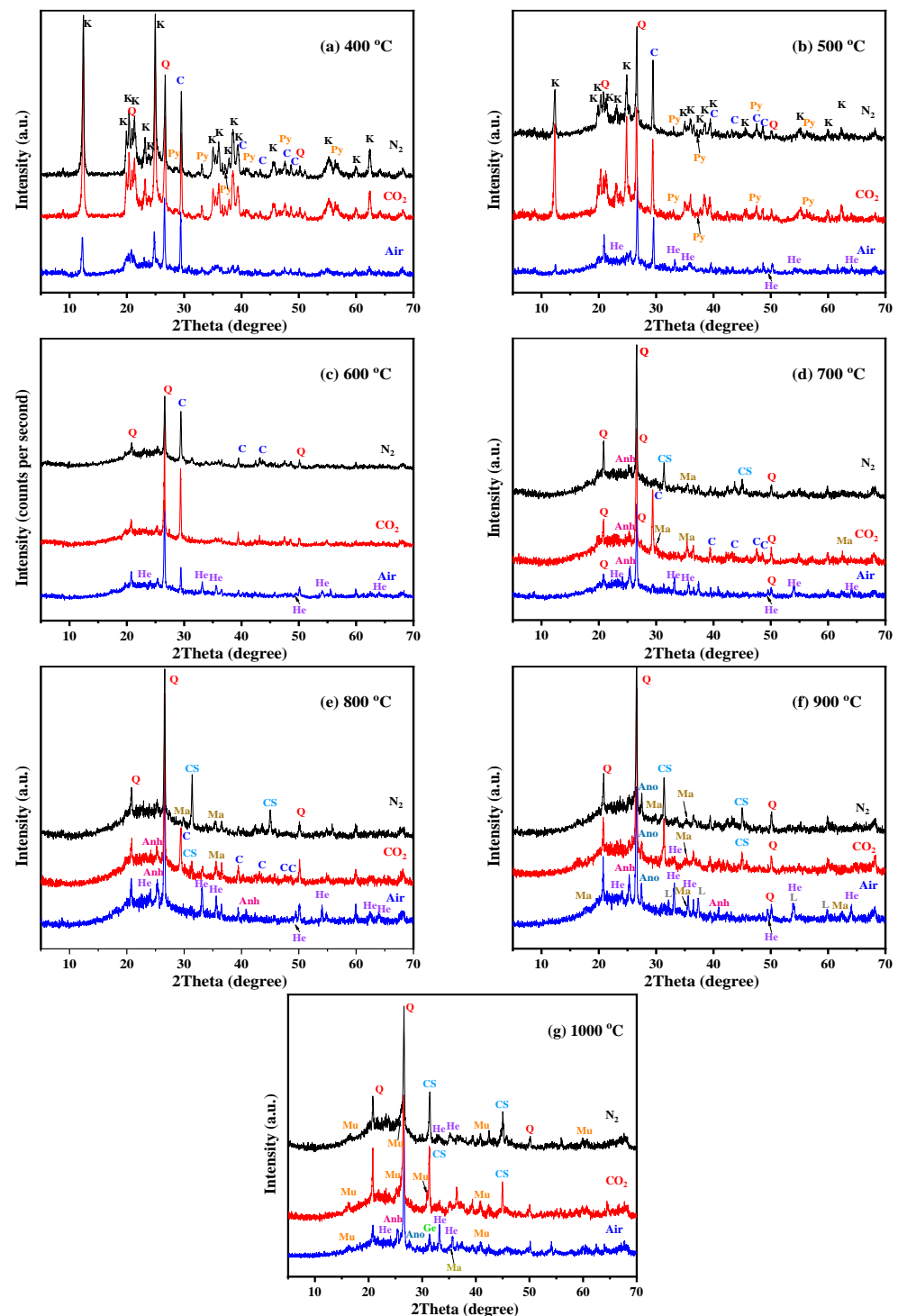


**Figure 5.** XRD pattern of the KAS calcined at 400 °C to 1000 °C under different atmospheres. (a) 400 °C, (b) 500 °C, (c) 600 °C, (d) 700 °C, (e) 800 °C, (f) 900 °C, (g) 1000 °C. (K—kaolinite, Q—quartz, C—calcite, Py—pyrite, He—hematite, Ma—magnetite, CS—calcium sulfate, Anh—anorthite, L—lime, Ge—gehlenite, Mu—mullite).

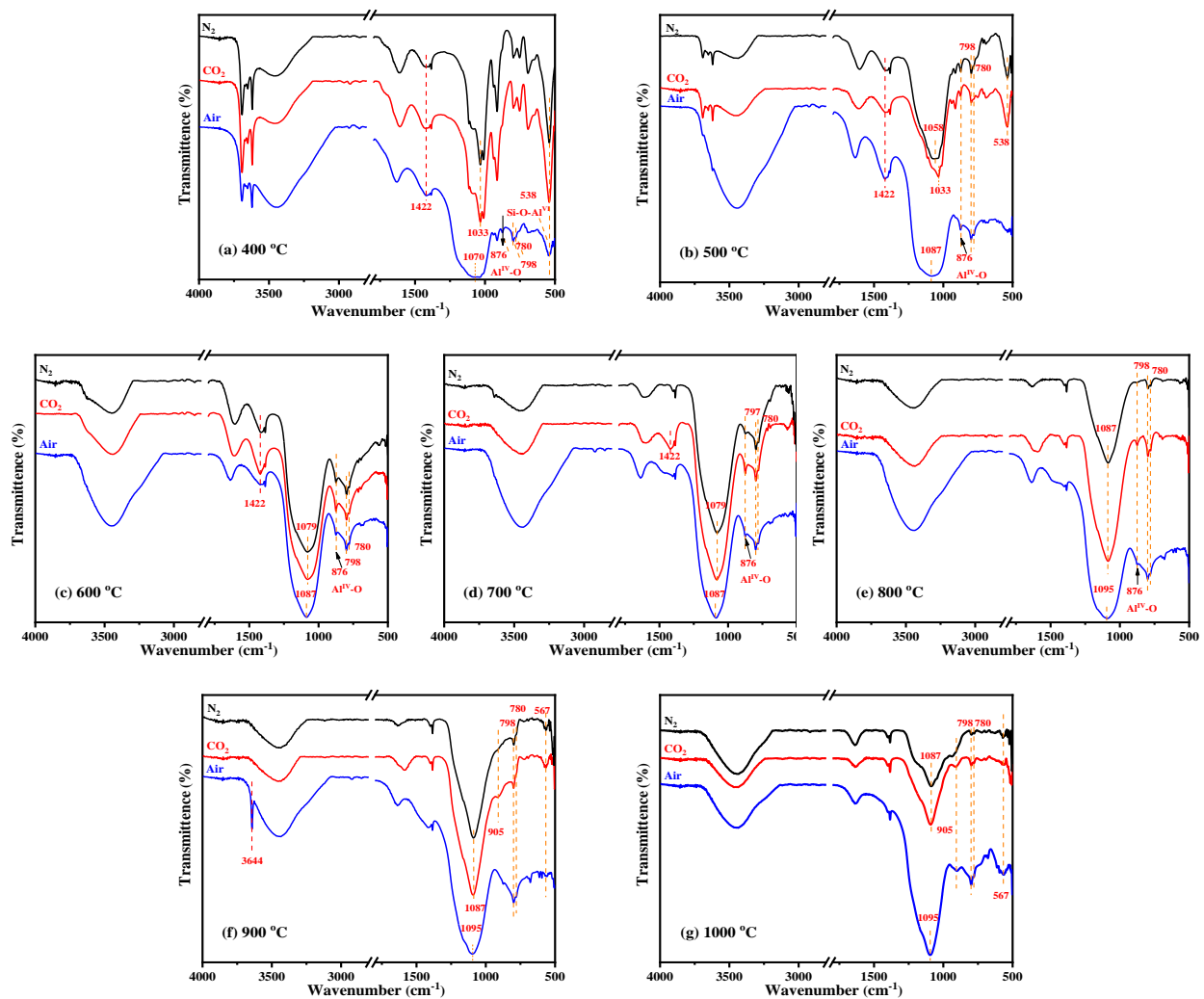


**Figure 6.** FTIR spectra of KAS calcined at 400 °C to 1000 °C under different atmospheres: (a) 400 °C, (b) 500 °C, (c) 600 °C, (d) 700 °C, (e) 800 °C, (f) 900 °C, (g) 1000 °C.

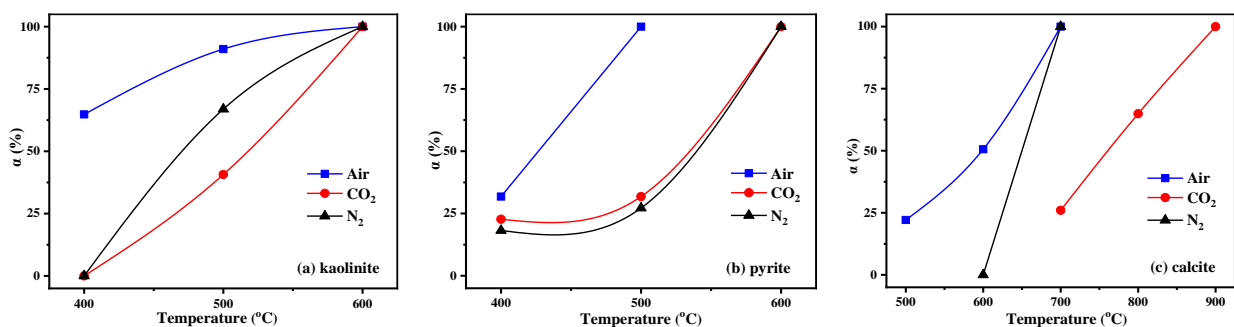


**Figure 7.** Relative decomposition rate of minerals in the KAS: (a) kaolinite, (b) pyrite, (c) calcite.

With the diffraction peak intensities of kaolinite disappearing at 600 °C, kaolinite was completely transformed into semicrystalline metakaolinite, which was maintained until 800 °C. At 800 °C, the broad Si-O and Al-O stretching bands continue redshifted (Figure 6e), indicating that the layer of metakaolinite became compact and began to sinter, and semicrystalline metakaolinite began to transform into amorphous aluminosilicate [28]. The schematic diagram is shown in Figure 9.

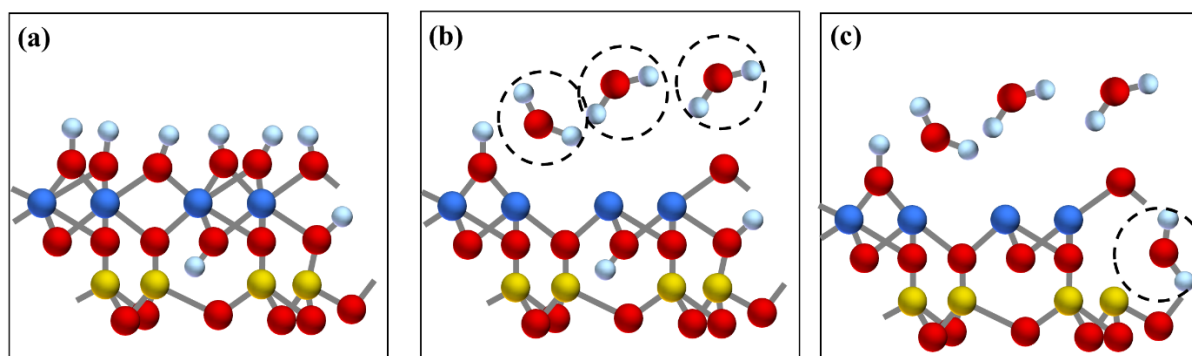


**Figure 8.** The mechanism schematic diagram of the transformation from kaolinite to metakaolinite by dehydroxylation: (a) layer structure of kaolinite, (b) escape of external hydroxyl group, (c) escape of internal hydroxyl group. Al, Si, O, and H atoms are represented by yellow, blue, red, and white spheres, respectively.

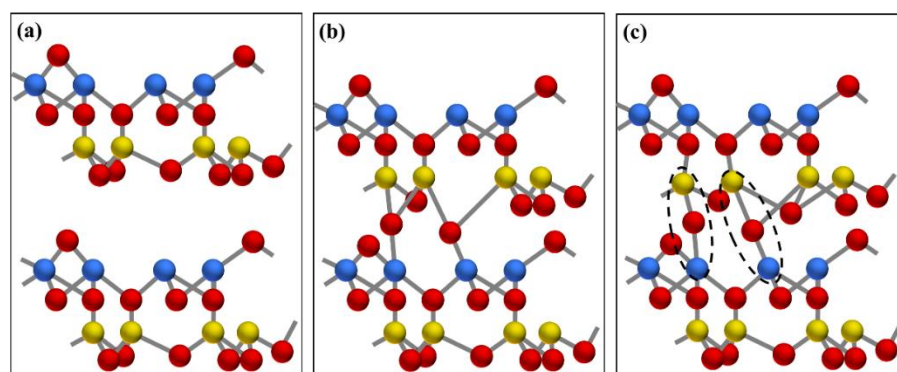


**Figure 9.** Schematic diagram of sintering between layers of metakaolinite: (a) layer structure of metakaolinite, (b) a high-energy transition state with an overcoordinated Si atom and Al–O bond dissociation, (c) a sintered structure with interlayer Al–O–Si bonds. Al, Si, and O atoms are represented by yellow, blue, and red spheres, respectively.

At 900 °C, the new phase anorthite appeared [33,45], which was formed by the free CaO (decomposition products of calcite) reacted with amorphous aluminosilicate according to the reaction (SI 19). Compared to Ca-poor coal mining waste, the calcite in the KAS lowered the beginning temperature of crystallization [46]. In addition, since the decomposition of calcite was restrained under the CO<sub>2</sub> atmosphere, the amount of neoformed anorthite was smaller than that formed under other atmospheres (Figure 6f). As the calcination temperature increased to 1000 °C, gehlenite and mullite formed, while anorthite decreased (reactions SI 20–21) [46,47].

From Figure 6f,g, it can be seen that the Si–O–Al<sup>IV</sup> peak at 876 cm<sup>−1</sup> disappeared after 900 °C, and new peaks appeared at 905 and 567 cm<sup>−1</sup>, also indicating the formation of new aluminosilicate minerals.

As for the minor mineral phases, the different transformations of pyrite and calcite were observed under different calcination temperatures and atmospheres. Under air atmosphere, with the disappearance of pyrite, hematite formed at 500 °C, and its peak intensities gradually increased from 500 to 800 °C. At 900 °C, a small amount of magnetite was generated and coexisted with hematite (reactions (SI 22–23)). Under N<sub>2</sub> and CO<sub>2</sub> atmospheres, the main mineral phase formed at 700 °C was magnetite, not hematite (reaction (SI 24)). This phenomenon was probably due to the different partial pressure of oxygen, and the higher partial pressure of oxygen promotes the formation of hematite [43,48].

With the decrease in the peak intensities of calcite, calcium sulfide generated at the same time as magnetite generated under both the N<sub>2</sub> and CO<sub>2</sub> atmospheres. However, due

to the participation of  $O_2$ , anhydrite generated at 700 °C under the air atmosphere (reaction (SI 25)).

### 3.4. The Chemical States of Silicon and Aluminum in Calcined KAS

The binding energy of Si 2p and Al 2p analyzed by XPS is determined by the chemical structure of silicon and aluminum. The binding energies of Si 2p and Al 2p of raw and calcined KASs under air atmosphere were investigated and are shown in Figure 10. The Si 2p binding energy for raw KAS is 102.92 eV, and it corresponds to silicon in the Si-O bond. The Al 2p binding energy for raw KAS is 74.72 eV, which can be assigned to Al in Al-OH [49]. Compared with raw KAS, the Si 2p binding energy for calcined KAS decreased at 700 °C, and then increased at 1000 °C under air atmosphere, while the Al 2p binding energy for calcined KAS increased at 700 and 1000 °C. The lowest Si 2p binding energy was achieved at 700 °C. This may be attributed to the fact that during calcination, the hydrogen bonds between the  $[SiO_4]$  tetrahedra sheet and the  $[AlO_6]$  octahedra sheet in the clay minerals were broken. Meanwhile, the VI-coordinated aluminum transformed into the more tightly connected IV-coordinated aluminum, which caused the Al 2p binding energy to increase slightly at 700 °C [25].

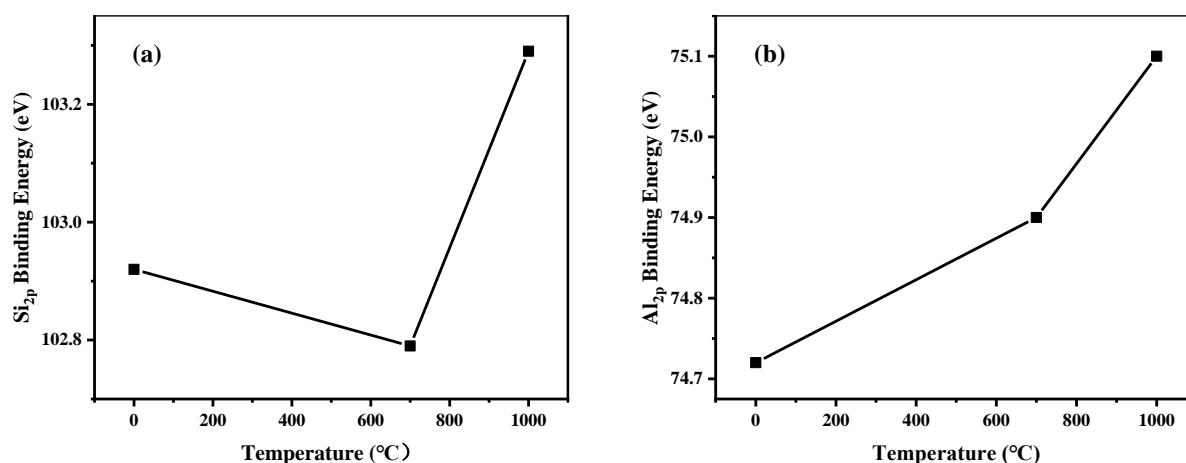


**Figure 10.** The binding energies of Si 2p and Al 2p for raw and calcined KAS under air atmosphere. (a) Si 2p, (b) Al 2p.

The detailed region scans of Al 2p and Si 2p of KAS calcined at 700 °C under different atmospheres are summarized in Figure 11. The binding energies for the Al 2p and Si 2p peaks did not change significantly when calcined under different atmospheres. However, a distinct variation in peak area indicated that a change in chemical structure might occur. It is well-known that the peak area of spectra for an atom relates to the fractional composition of this atom, and thus the atomic ratios of Si to Al can be calculated by the aid of the atomic sensitivity factors ( $ASF(Al\ 2p) = 0.185$  and  $ASF(Si\ 2p) = 0.270$ ) (Table 5) [7]. It can be seen that the peak area for KAS calcined under air showed a different changing pattern from KAS calcined under  $N_2$  and  $CO_2$ . Compared with raw KAS, the peak areas of both Al 2p and Si 2p calcined under air nearly doubled, while the peak areas calcined under  $N_2$  and  $CO_2$  slightly decreased. The detected atomic ratio of Si to Al in the raw KAS was 1.2, which showed small deviations from the bulk atomic ratio of Si to Al, determined from the XRF analysis, implying that the KAS was well-distributed. Furthermore, few variations in the atomic ratio of Si to Al could be observed after the KAS calcined in different atmospheres. Therefore, the significant increase in the peak area of Al 2p and Si 2p calcined under air might be the result of the burning out of carbon on the surface of KAS.

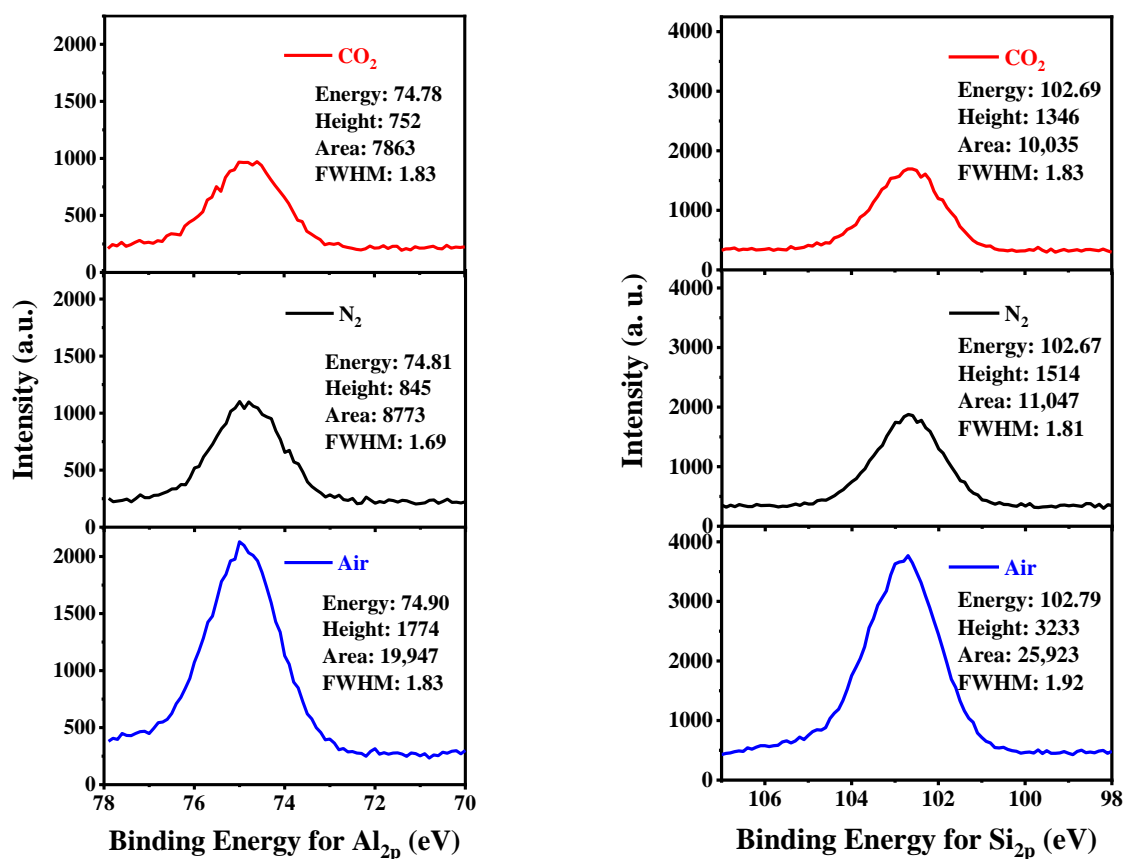


Figure 11. Al 2p and Si 2p photoelectron spectra of KAS calcined at 700 °C under different atmospheres.

Table 5. The changes in peak areas and the atomic ratios of Si to Al of the samples.

Sample	Atom Type	Peak Area Ratio	Si/Al
A-KAS-700	Al 2p	1.96	1.30
	Si 2p	2.13	
N-KAS-700	Al 2p	0.86	1.26
	Si 2p	0.91	
C-KAS-700	Al 2p	0.77	1.28
	Si 2p	0.82	

### 3.5. Leaching Tests Analysis of Calcined KAS

The leaching rates of Al<sub>2</sub>O<sub>3</sub> and SiO<sub>2</sub> in raw KAS were determined to be only 4.2% and 3.7%, respectively. This result showed that the chemical reactivity of the raw KAS is very low, which is caused by the carbon and minerals of the crystalline structure in KAS [8]. Therefore, it is necessary to improve the chemical reactivity by calcination.

The leaching rates of the Al<sub>2</sub>O<sub>3</sub> and SiO<sub>2</sub> of KAS calcined under different treatment conditions are summarized in Figure 12. Compared with raw KAS, the leaching rates of Al<sub>2</sub>O<sub>3</sub> and SiO<sub>2</sub> were greatly improved by calcination. The calcination treatment led to consistent changes in the leaching rates of Al<sub>2</sub>O<sub>3</sub> and SiO<sub>2</sub> for the three calcination atmospheres assessed. The leaching rates increased with the increase in calcination temperature up to 600–700 °C, and then it suddenly decreased after 800 °C. Moreover, the leaching rates of Al<sub>2</sub>O<sub>3</sub> and SiO<sub>2</sub> in the KAS calcined under air were significantly higher than those of the KAS calcined under N<sub>2</sub> and CO<sub>2</sub> atmospheres. The results in Figure 10 show that the Al<sub>2</sub>O<sub>3</sub> and SiO<sub>2</sub> leaching rates of calcinated KAS reached a maximum at 700 °C under air atmosphere, which were 90.4% and 84.0%, respectively. Under the N<sub>2</sub> and CO<sub>2</sub> atmospheres, the Al<sub>2</sub>O<sub>3</sub> and SiO<sub>2</sub> leaching rates reached a maximum of 600 °C

and were 79.7% and 77.7% under the  $N_2$  atmosphere, and 79.8% and 78.5% under the  $CO_2$  atmosphere.

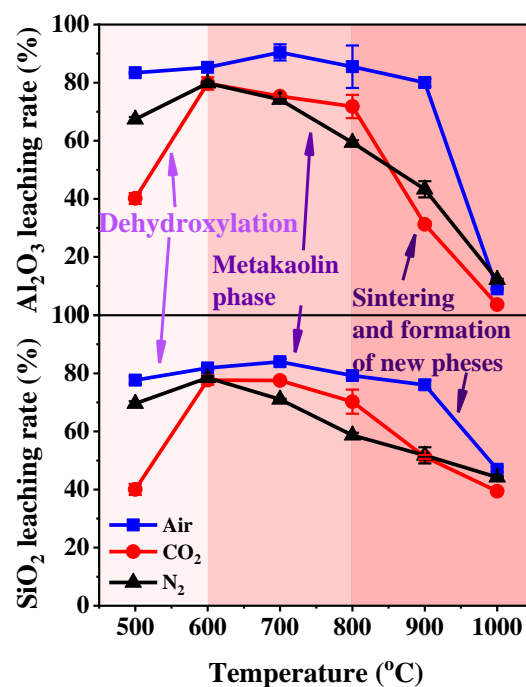


Figure 12. The leaching rate of  $Al_2O_3$  and  $SiO_2$  in calcined KAS.

### 3.6. Thermal Activation Mechanism of KAS

The leaching results manifest the connection between the structural transformation and chemical reactivity of the KAS during calcination. The relatively higher  $Al_2O_3$  and  $SiO_2$  leaching rate at 600–800 °C indicated that the KAS calcined at 600–800 °C exhibited higher chemical reactivity. The leaching rate of  $Al_2O_3$  and  $SiO_2$  decreased after 800 °C, which showed that the chemical reactivity of the calcined KAS lowered after 800 °C. These results are consistent with the change in the transformation of kaolinite during the calcination of the KAS.

Various structure transformations of kaolinite corresponding to the different chemical reactivities were identified. Before 400 °C, crystalline kaolinite was observed. Due to the existence of structural hydroxyl groups and the stable Al-O bonds and Si-O bonds in the network structures of kaolinite, the chemical reactivity of the KAS was very low. From 400 to 600 °C, dehydroxylation gradually decomposed kaolinite to the semicrystalline metakaolinite. The transformation from a stable structure into a non-stable structure accounted for the increase in chemical reactivity. In the range of 600–800 °C, the complete transformation of metakaolinite resulted in the highest chemical reactivity. Beyond 800 °C, layers of metakaolinite began to sinter, while anorthite, gehlenite, and mullite phases subsequently appeared. The appearance of a structure more stable than metakaolinite led to the decrease in chemical reactivity.

Apart from the structural transformation of kaolinite, the carbon content in the KAS also affects chemical reactivity. Before 600 °C, the accelerated transformation of kaolinite caused by combustion of carbon in the KAS resulted in the higher leaching rates of the calcinated samples than the KAS samples under air than those under other atmospheres. Beyond 600 °C, although the complete transition of kaolinite to metakaolinite occurred under each atmosphere, the leaching rates of calcinated KAS under air were still higher than those under inert atmospheres. This was because when the KAS calcinated under inert atmospheres, the carbon only pyrolyzed to form semi-coke. The existence of semi-coke increased the resistance of mass transfer and solid–liquid separation in the leaching reaction, thereby decreasing the leaching rate [6].

#### 4. Conclusions

In this paper, the structural evolution of carbon and minerals derived from the KAS and its chemical reactivity during calcination have been systematically studied. The results show that the applied KAS mainly consisted of kaolinite and carbon, with a small amount of quartz, calcite, and pyrite, and presented weak chemical reactivity. It was determined that KAS calcination under air atmosphere can burn out carbon at 650 °C, while the combustion of carbon is conducive to the low-temperature decomposition of kaolinite, calcite, and pyrite. However, calcination under N<sub>2</sub> and CO<sub>2</sub> atmospheres results in a char residual. Moreover, the structural transformation of kaolinite during calcination includes dehydroxylation, sintering, and the formation of anorthite, gehlenite, and mullite. Furthermore, calcination greatly improves the chemical reactivity of KAS as a result of the dehydroxylation of crystalline kaolinite, and the KAS calcined at 600–800 °C shows high chemical reactivity. On the other hand, the decrease in chemical reactivity after 800 °C is attributed to the interlayer sintering of metakaolinite and the recrystallization of amorphous components. Additionally, the presence of carbon reduces the chemical reactivity of calcined KAS.

**Supplementary Materials:** The following supporting information can be downloaded at: <https://www.mdpi.com/article/10.3390/min13040466/s1>.

**Author Contributions:** Conceptualization, X.D.; methodology, X.D.; investigation, H.X.; resources, X.M.; data curation, H.X.; writing—original draft preparation, H.X.; writing—review and editing, X.D. and S.Y.; supervision, Y.F.; project administration, Y.F.; funding acquisition, X.M. All authors have read and agreed to the published version of the manuscript.

**Funding:** This work was supported by the International Cooperation and Exchange of the National Natural Science Foundation of China (Grant No. 51820105006); the National Natural Science Foundation of China (Grant No. 52004178); the Natural Science Foundation of Applied Basic Research Project in Shanxi Province (Grant No. 201901D111075); the Graduate Education Innovation Project in Shanxi Province (Grant No. 2020BY149); and the Fund Program for the Scientific Activities of Selected Returned Overseas Professionals in Shanxi Province.

**Data Availability Statement:** Data not available due to privacy restrictions.

**Conflicts of Interest:** The authors declare no conflict of interest.

#### References

1. Zhang, Y.; Ling, T.-C. Reactivity activation of waste coal gangue and its impact on the properties of cement-based materials—A review. *Constr. Build. Mater.* **2020**, *234*, 117424. [\[CrossRef\]](#)
2. Hollanders, S.; Adriaens, R.; Skibsted, J.; Cizer, Ö.; Elsen, J. Pozzolanic reactivity of pure calcined clays. *Appl. Clay Sci.* **2016**, *132–133*, 552–560. [\[CrossRef\]](#)
3. Li, Y.; Yao, Y.; Liu, X.; Sun, H.; Ni, W. Improvement on pozzolanic reactivity of coal gangue by integrated thermal and chemical activation. *Fuel* **2013**, *109*, 527–533. [\[CrossRef\]](#)
4. Liu, D.; Huang, Y.; Hu, J.; Feng, Q.; Xiao, J. Thermal activation mechanism and pozzolanic activity characteristics of coal flotation tailing. *Adv. Cem. Res.* **2021**, *33*, 145–155. [\[CrossRef\]](#)
5. Balczár, I.; Korim, T.; Kovács, A.; Makó, É. Mechanochemical and thermal activation of kaolin for manufacturing geopolymer mortars—Comparative study. *Ceram. Int.* **2016**, *42*, 15367–15375. [\[CrossRef\]](#)
6. Dong, L.; Liang, X.; Song, Q.; Gao, G.; Song, L.; Shu, Y.; Shu, X. Study on Al<sub>2</sub>O<sub>3</sub> extraction from activated coal gangue under different calcination atmospheres. *J. Therm. Sci.* **2017**, *26*, 570–576. [\[CrossRef\]](#)
7. Guo, Y.; Yan, K.; Cui, L.; Cheng, F. Improved extraction of alumina from coal gangue by surface mechanically grinding modification. *Powder Technol.* **2016**, *302*, 33–41. [\[CrossRef\]](#)
8. Han, L.; Ren, W.; Wang, B.; He, X.; Ma, L.; Huo, Q.; Wang, J.; Bao, W.; Chang, L. Extraction of SiO<sub>2</sub> and Al<sub>2</sub>O<sub>3</sub> from coal gangue activated by supercritical water. *Fuel* **2019**, *253*, 1184–1192. [\[CrossRef\]](#)
9. Lin, M.; Liu, Y.-Y.; Lei, S.-M.; Ye, Z.; Pei, Z.-Y.; Li, B. High-efficiency extraction of Al from coal-series kaolinite and its kinetics by calcination and pressure acid leaching. *Appl. Clay Sci.* **2018**, *161*, 215–224. [\[CrossRef\]](#)
10. Li, T.; Liu, H.; Fan, Y.; Yuan, P.; Shi, G.; Bi, X.T.; Bao, X. Synthesis of zeolite Y from natural aluminosilicate minerals for fluid catalytic cracking application. *Green Chem.* **2012**, *14*, 3255–3259. [\[CrossRef\]](#)
11. Dong, Z.; Xia, J.; Fan, C.; Cao, J. Activity of calcined coal gangue fine aggregate and its effect on the mechanical behavior of cement mortar. *Constr. Build. Mater.* **2015**, *100*, 63–69. [\[CrossRef\]](#)

12. Jin, Y.; Li, L.; Liu, Z.; Zhu, S.; Wang, D. Synthesis and characterization of low-cost zeolite NaA from coal gangue by hydrothermal method. *Adv. Powder Technol.* **2021**, *32*, 791–801. [\[CrossRef\]](#)
13. Lu, X.; Shi, D.; Chen, J. Sorption of Cu<sup>2+</sup> and Co<sup>2+</sup> using zeolite synthesized from coal gangue: Isotherm and kinetic studies. *Environ. Earth Sci.* **2017**, *76*, 591. [\[CrossRef\]](#)
14. Maia, A.Á.B.; Angélica, R.S.; de Freitas Neves, R.; Pöllmann, H.; Straub, C.; Saalwächter, K. Use of <sup>29</sup>Si and <sup>27</sup>Al MAS NMR to study thermal activation of kaolinites from Brazilian Amazon kaolin wastes. *Appl. Clay Sci.* **2014**, *87*, 189–196. [\[CrossRef\]](#)
15. Autef, A.; Joussein, E.; Gasgnier, G.; Pronier, S.; Sobrados, I.; Sanz, J.; Rossignol, S. Role of metakaolin dehydroxylation in geopolymer synthesis. *Powder Technol.* **2013**, *250*, 33–39. [\[CrossRef\]](#)
16. Frías, M.; la Villa, R.V.; Rojas, M.I.S.; Medina, C.; Juan Valdés, A.; Jantzen, C. Scientific Aspects of Kaolinite Based Coal Mining Wastes in Pozzolan/Ca(OH)<sub>2</sub> System. *J. Am. Ceram. Soc.* **2012**, *95*, 386–391. [\[CrossRef\]](#)
17. Alam, N.; Ozdemir, O.; Hampton, M.A.; Nguyen, A.V. Dewatering of coal plant tailings: Flocculation followed by filtration. *Fuel* **2011**, *90*, 26–35. [\[CrossRef\]](#)
18. Chen, R.; Dong, X.; Fan, Y.; Ma, X.; Dong, Y.; Chang, M. Interaction between STAC and coal/kaolinite in tailing dewatering: An experimental and molecular-simulation study. *Fuel* **2020**, *279*, 118224. [\[CrossRef\]](#)
19. BP Plc. *Statistical Review of World Energy 2021*; BP Plc: London, UK, 2021.
20. *2020 China Ecological Environment Statistics Annual Report*; Ministry of Ecology and Environment of the People's Republic of China: Beijing, China, 2022.
21. Furnell, E.; Bilaniuk, K.; Goldbaum, M.; Shoaib, M.; Wani, O.; Tian, X.; Chen, Z.; Boucher, D.; Bobicki, E.R. Dewatered and Stacked Mine Tailings: A Review. *ACS EST Eng.* **2022**, *2*, 728–745. [\[CrossRef\]](#)
22. Fallavena, V.L.V.; Pires, M.; Ferrarini, S.F.; Silveira, A.P.B. Evaluation of Zeolite/Backfill Blend for Acid Mine Drainage Remediation in Coal Mine. *Energy Fuels* **2018**, *32*, 2019–2027. [\[CrossRef\]](#)
23. Deng, J.; Li, B.; Xiao, Y.; Ma, L.; Wang, C.-P.; Lai-wang, B.; Shu, C.-M. Combustion properties of coal gangue using thermogravimetry–Fourier transform infrared spectroscopy. *Appl. Therm. Eng.* **2017**, *116*, 244–252. [\[CrossRef\]](#)
24. Zhang, Y.; Zhang, Z.; Zhu, M.; Cheng, F.; Zhang, D. Decomposition of key minerals in coal gangues during combustion in O<sub>2</sub>/N<sub>2</sub> and O<sub>2</sub>/CO<sub>2</sub> atmospheres. *Appl. Therm. Eng.* **2019**, *148*, 977–983. [\[CrossRef\]](#)
25. Zhang, Y.; Xu, L.; Seetharaman, S.; Liu, L.; Wang, X.; Zhang, Z. Effects of chemistry and mineral on structural evolution and chemical reactivity of coal gangue during calcination: Towards efficient utilization. *Mater. Struct.* **2014**, *48*, 2779–2793. [\[CrossRef\]](#)
26. Xu, B.; Liu, Q.; Ai, B.; Ding, S.; Frost, R.L. Thermal decomposition of selected coal gangue. *J. Therm. Anal. Calorim.* **2017**, *131*, 1413–1422. [\[CrossRef\]](#)
27. Yuan, S.; Li, Y.; Han, Y.; Gao, P. Effects of carbonaceous matter additives on kinetics, phase and structure evolution of coal-series kaolin during calcination. *Appl. Clay Sci.* **2018**, *165*, 124–134. [\[CrossRef\]](#)
28. Muraleedharan, M.G.; Asgar, H.; Mohammed, S.; Gadikota, G.; van Duin, A.C.T. Elucidating thermally induced structural and chemical transformations in kaolinite using reactive molecular dynamics simulations and X-ray scattering measurements. *Chem. Mater.* **2019**, *32*, 651–662. [\[CrossRef\]](#)
29. Bich, C.; Ambroise, J.; Péra, J. Influence of degree of dehydroxylation on the pozzolanic activity of metakaolin. *Appl. Clay Sci.* **2009**, *44*, 194–200. [\[CrossRef\]](#)
30. Zhang, Z.; Wang, H.; Yao, X.; Zhu, Y. Effects of halloysite in kaolin on the formation and properties of geopolymers. *Cement Concrete Comp.* **2012**, *34*, 709–715. [\[CrossRef\]](#)
31. Wei, B.; Liu, H.; Li, T.; Cao, L.; Fan, Y.; Bao, X. Natural rectorite mineral: A promising substitute of kaolin for in-situ synthesis of fluid catalytic cracking catalysts. *AIChE J.* **2010**, *56*, 2913–2922. [\[CrossRef\]](#)
32. Zhou, C.; Liu, G.; Yan, Z.; Fang, T.; Wang, R. Transformation behavior of mineral composition and trace elements during coal gangue combustion. *Fuel* **2012**, *97*, 644–650. [\[CrossRef\]](#)
33. Giménez-García, R.; Vigil de la Villa Mencía, R.; Rubio, V.; Frías, M. The transformation of coal-mining waste minerals in the pozzolanic reactions of cements. *Minerals* **2016**, *6*, 64. [\[CrossRef\]](#)
34. Zhang, N.; Liu, X.; Sun, H.; Li, L. Pozzolanic behaviour of compound-activated red mud-coal gangue mixture. *Cem. Concr. Res.* **2011**, *41*, 270–278. [\[CrossRef\]](#)
35. Liu, Y.; Lei, S.; Lin, M.; Li, Y.; Ye, Z.; Fan, Y. Assessment of pozzolanic activity of calcined coal-series kaolin. *Appl. Clay Sci.* **2017**, *143*, 159–167. [\[CrossRef\]](#)
36. Cao, Z.; Cao, Y.; Dong, H.; Zhang, J.; Sun, C. Effect of calcination condition on the microstructure and pozzolanic activity of calcined coal gangue. *Int. J. Miner. Process.* **2016**, *146*, 23–28. [\[CrossRef\]](#)
37. Li, L.; Zhang, Y.; Zhang, Y.; Sun, J.; Hao, Z. The thermal activation process of coal gangue selected from Zhungeer in China. *J. Therm. Anal. Calorim.* **2016**, *126*, 1559–1566. [\[CrossRef\]](#)
38. Li, L.; Zhang, Y.; Zhang, Y.; Sun, J.; Wang, Z. The thermal transmission behavior analysis of two coal gangues selected from inner Mongolia in China. *Therm. Sci.* **2018**, *22*, 1111–1119. [\[CrossRef\]](#)
39. Li, C.; Wan, J.; Sun, H.; Li, L. Investigation on the activation of coal gangue by a new compound method. *J. Hazard. Mater.* **2010**, *179*, 515–520. [\[CrossRef\]](#)
40. Wang, Y.; Zhang, Y.; Zhou, Q.; Zhang, Y.; Sun, J. Thermal kinetics analysis of coal-gangue selected from Inner Mongolia in China. *J. Therm. Anal. Calorim.* **2017**, *131*, 1835–1843. [\[CrossRef\]](#)

41. Jayaraman, K.; Kok, M.V.; Gokalp, I. Pyrolysis, combustion and gasification studies of different sized coal particles using TGA-MS. *Appl. Therm. Eng.* **2017**, *125*, 1446–1455. [[CrossRef](#)]
42. Wu, J.; Wang, B.; Cheng, F. Thermal and kinetic characteristics of combustion of coal sludge. *J. Therm. Anal. Calorim.* **2017**, *129*, 1899–1909. [[CrossRef](#)]
43. Meng, F.; Yu, J.; Tahmasebi, A.; Han, Y. Pyrolysis and combustion behavior of coal gangue in O<sub>2</sub>/CO<sub>2</sub> and O<sub>2</sub>/N<sub>2</sub> mixtures using thermogravimetric analysis and a drop tube furnace. *Energy Fuels* **2013**, *27*, 2923–2932. [[CrossRef](#)]
44. Guo, Y.; Yan, K.; Cui, L.; Cheng, F.; Lou, H.H. Effect of Na<sub>2</sub>CO<sub>3</sub> additive on the activation of coal gangue for alumina extraction. *Int. J. Miner. Process.* **2014**, *131*, 51–57. [[CrossRef](#)]
45. Zimmer, A.; Bergmann, C.P. Fly ash of mineral coal as ceramic tiles raw material. *Waste Manag.* **2007**, *27*, 59–68. [[CrossRef](#)]
46. Trindade, M.; Dias, M.; Coroado, J.; Rocha, F. Mineralogical transformations of calcareous rich clays with firing: A comparative study between calcite and dolomite rich clays from Algarve, Portugal. *Appl. Clay Sci.* **2009**, *42*, 345–355. [[CrossRef](#)]
47. Lei, M.; Zou, C.; Xu, X.; Wang, C. Effect of CO<sub>2</sub> and H<sub>2</sub>O on the combustion characteristics and ash formation of pulverized coal in oxy-fuel conditions. *Appl. Therm. Eng.* **2018**, *133*, 308–315. [[CrossRef](#)]
48. Ilham, D.; Randall, E.H.; Philip, J.D. Formation and use of coal combustion residues from three types of power plants burning Illinois coals. *Fuel* **2001**, *80*, 1659–1673.
49. Zhang, N.; Ejtemaei, M.; Nguyen, A.V.; Zhou, C. XPS analysis of the surface chemistry of sulfuric acid-treated kaolinite and diasporite minerals with flotation reagents. *Miner. Eng.* **2019**, *136*, 1–7. [[CrossRef](#)]

**Disclaimer/Publisher’s Note:** The statements, opinions and data contained in all publications are solely those of the individual author(s) and contributor(s) and not of MDPI and/or the editor(s). MDPI and/or the editor(s) disclaim responsibility for any injury to people or property resulting from any ideas, methods, instructions or products referred to in the content.